

Silicon nanocolumn-based disposable and flexible ultrasound patches

Received: 2 December 2024

Accepted: 4 July 2025

Published online: 18 July 2025



Dong-Hyun Kang^{1,2,9}, Seonghun Cho^{1,3,9}, Hae Youn Kim¹, Shinyong Shim¹, Dong Hun Kim¹, Baren Jeong⁴, Yoon Seong Lee⁴, Eun-Ah Park⁴, Whal Lee⁴, Hyungmin Kim¹, Butrus T. Khuri-Yakub⁵, Maesoon Im^{6,7,8}, Jae-Woong Jeong³✉ & Byung Chul Lee^{1,7,8}✉

Traditional wearable ultrasound devices pose challenges concerning the rigidity and environmental impact of lead-based piezoelectric materials. This study proposes a silicon nanocolumn capacitive micromachined ultrasonic transducer (snCMUT) array for real-time wearable ultrasound imaging in disposable patches. Using a lead-free design, snCMUT incorporates silicon nanocolumns to address existing issues and achieves high transmission efficiency (220 kPa/V), flexibility, and low power consumption. The specialized structure of snCMUT enhances displacement efficiency, enabling high-resolution imaging while maintaining a thin, flexible form factor (~900 μm). Phantom imaging demonstrates its superior performance, with high axial and lateral resolutions (0.52 and 0.55 mm) and depth penetration (~70 mm) at low voltage (8.9 V_{pp}). Upon successful application to monitor both sides of the human carotid arteries, snCMUT offers clear ultrasound images and continuous blood pressure waveform monitoring. This proposed innovation presents significant potential for continuous medical imaging and cardiovascular health assessment, addressing environmental concerns and reducing manufacturing costs (<\$20).

Ultrasound is a widely used medical imaging modality, providing non-invasive and safe real-time imaging of deep-lying tissues, organs, and blood flow^{1–3}. Compared to X-ray, computed tomography (CT), and magnetic resonance imaging (MRI), ultrasound machines are relatively compact and inexpensive^{3–5}. Recent advancements in wearable devices and technology have led to the development of wearable ultrasonic transducer arrays^{1,4,6–15}, which enable various applications, including monitoring blood flow in different body regions, imaging cardiovascular structures, and mapping tissue moduli.

However, wearable ultrasound devices pose issues related to their inherent material limitations. First, as the primary component of wearable ultrasound devices, piezoelectric materials predominantly containing lead pose environmental issues and violate the Restriction of Hazardous Substances Directive (RoHS). Second, the inherent properties of piezoelectric materials necessitate thick backing layers to define ultrasound propagation direction and minimize pulse duration while quickly damping vibrations^{14,16}. When backing layers are insufficient, both axial and lateral resolution worsen due to the ringing

¹Bionics Research Center, Korea Institute of Science and Technology, Seongbuk-gu, Seoul, Republic of Korea. ²Department of Mechanical Engineering, Gangneung-Wonju National University, Wonju, Gangwon-do, Republic of Korea. ³School of Electrical Engineering, Korea Advanced Institute of Science and Technology, Yuseong-gu, Daejeon, Republic of Korea. ⁴Department of Radiology, Seoul National University Hospital, Jongno-gu, Seoul, Republic of Korea. ⁵Department of Electrical Engineering, Stanford University, Stanford, CA, USA. ⁶Brain Science Institute, Korea Institute of Science and Technology, Seongbuk-gu, Seoul, Republic of Korea. ⁷Division of Bio-Medical Science and Technology, KIST School, Korea National University of Science and Technology, Seongbuk-gu, Seoul, Republic of Korea. ⁸KHU-KIST Department of Converging Science and Technology, Kyung Hee University, Dongdaemun-gu, Seoul, Republic of Korea. ⁹These authors contributed equally: Dong-Hyun Kang, Seonghun Cho. ✉e-mail: jeong1@kaist.ac.kr; bclee@kist.re.kr

and reverberation of transducers. The thick layers make them unsuitable for wearable ultrasound technology, especially wearable patches for continuous monitoring, as they introduce discomfort when attached to the body. Third, assembling rigid piezoelectric materials with flexible electrodes to achieve conformal contact becomes increasingly difficult as array size and density increase due to fabrication based on blade dicing^{4,17}. Thus, obstacles arise in medical imaging fields requiring narrow pitch, minimized kerf, and numerous elements to achieve high-resolution imaging attributable to the transducer beam width. Last, the high production cost of ultrasound transducer arrays typically necessitates the reuse of wearable patch-type ultrasound probes, driven by economic challenges^{16,18}. While the reuse of ultrasound probes with disposable medical cover is standard in medical imaging, primarily due to the high production cost and environmental issues associated with lead-based piezoelectric materials, the concept of disposable ultrasound probes offers compelling advantages to wearable patches. Disposable ultrasound probes address hygiene, infection control, and cross-contamination issues in medical environments, thereby alleviating the burden of cleaning and sterilization between uses and offering convenience and cost-effectiveness to healthcare providers and patients. Particularly, disposable ultrasound probes enhance patient safety and eliminate the need for sterilization to streamline diagnostic procedures in environments following stringent hygiene protocols.

Based on silicon wafers and semiconductor fabrication technology, capacitive micromachined ultrasonic transducers (CMUTs) offer a lead-free alternative to piezoelectric material-based ultrasound transducers with considerable potential for medical imaging, as they boast high element density and enable miniaturization advantages^{2,3,19}. Free from lead, CMUTs circumvent environmental regulations, while batch production capabilities drastically reduce manufacturing costs even with high element density (under \$12, Supplementary Table 1), facilitating the realization of disposable ultrasound probe patches. Moreover, CMUTs offer superior sensitivity, image resolution, and bandwidth compared to conventional piezoelectric material-based ultrasound probes^{2,3,20}. Unlike piezoelectric transducers that experience degraded piezoelectric characteristics and signal-to-noise ratio (SNR) due to their rising temperature during long-term use, CMUTs avoid temperature increases even during extended use, making them more suitable for wearable patches intended for long-term monitoring²¹. However, despite the potential of CMUTs for high-resolution ultrasound imaging in wearable patches, their adoption faces challenges, including low output pressure and high bias voltage, which limit imaging depth and elevate driving voltage^{22,23}.

This study presents a flexible CMUT with exceptional pressure output, designed for real-time wearable ultrasound imaging in disposable patches (Fig. 1a). Leveraging semiconductor and micro-machining technologies, the designed lead-free ultrasound patches based on silicon nanocolumn capacitive micromachined ultrasonic transducer (snCMUT) array are disposable and environmentally friendly, with minimized fabrication costs of under \$20 (Supplementary Table 1). The skin-conformal ultrasound patch comprises individual flexible CMUT elements separated by elastomer-filled trenches, mounted on an in-house designed flexible printed circuit board (FPCB), and encapsulated with polydimethylsiloxane (PDMS) (Fig. 1b). To enhance transmission efficiency and reduce power consumption, silicon nanocolumns are utilized as springs beneath the moving plate of snCMUT, increasing the average displacement (Fig. 1c). Fabricated using a rigid-island technique, the snCMUT array boasts high flexibility (minimum radius of curvature: <1 mm), stretchability (up to 140% without degradation), and minimized thickness (~900 µm fully packaged), making it ideal for wearable applications (Fig. 1d, e). To demonstrate the capabilities of disposable snCMUT patches, the human carotid artery is monitored on both sides of the neck in real-time. Owing to its elevated transmission efficiency, disposable

snCMUT patches produce clear ultrasound images (B-mode for sonography and M-mode for blood pressure wave, Fig. 1f) even at low driving voltages (8.9 V_{pp}, Supplementary Table 2). The cost-effective disposable snCMUT patches enable multi-point monitoring of blood pressure waveforms, offering significant clinical advantages for cardiovascular health assessment and management. By monitoring both carotid arteries simultaneously, disposable snCMUT patches assist in identifying hypertensive patients missed with single-side measurements, detecting asymmetrical arterial stiffness, guiding precise treatment plans, enhancing patient safety, and supporting surgical planning and postoperative evaluation^{24,25}.

Results and discussion

Fabrication of flexible snCMUT arrays

The proposed snCMUT operates on a principle different from that of conventional CMUTs, which rely on the deformation of a thin plate^{19,20}. In the design, snCMUTs use a thin plate with pistons driven by silicon nanocolumns as a spring^{26,27}. The structure introduces a spring constant in the mass-spring-damper system, enhancing average displacement and packing density through parallel piston movement and large unit cells, respectively (Fig. 2a, b, left). Finite element analysis (FEA) simulations provide design parameters of the CMUT structure with silicon nanocolumns, aiming for a resonant frequency of 5 MHz for carotid artery imaging (Fig. 2a, b, right). Since conventional CMUTs offer a pull-in voltage of 93 V, while snCMUT exhibits the pull-in voltage of 105 V, we applied normalized voltages at 0%, 20%, 40%, 60%, 80%, and 95% of the respective pull-in voltages of each transducer. The results confirmed that the snCMUT exhibits significantly greater plate deflection than the conventional CMUT enabling much higher transmission efficiency for high resolution ultrasound imaging. The design includes 20 piston top plates forming a CMUT element, each affixed with nine 2 µm long silicon nanocolumns. To integrate vertically oriented silicon nanocolumns into CMUTs, precise fabrication with specific dimensions is necessary. Thus, compatibility with CMUT fabrication is crucial, favouring a top-down approach via silicon wafer etching over a bottom-up approach.

Using deep reactive ion etching (DRIE) and reactive ion etching (RIE), silicon nanocolumns were fabricated with fixed central diameters of 1.5 µm and varying doughnut-shaped widths to control etch rates (Fig. 2c). Silicon microcolumns of 1.45 µm diameter and scalloped sidewalls were fabricated using DRIE (Fig. 2d, Supplementary Fig. 1a). While fabricating nanocolumns by reducing the silicon microcolumn size through RIE undercutting, precise control of the vertical and horizontal etch rate (984 and 758 Å/min, respectively, for this study) was crucial. The uniformity of etching anisotropy was confirmed even with increased etching time, and the undercut was controlled by varying the opening area (W) and etch time (Supplementary Fig. 2). Successful top-down fabrication of silicon nanocolumns (Fig. 2e, Supplementary Fig. 1b–d) with diameters controlled by etch time was achieved (Fig. 2f). The mechanical properties of the silicon nanocolumns, acting as springs, were evaluated using a pico-indenter. Smaller diameter nanocolumns contracted more, with 300 nm diameter nanocolumns changing length by 148 nm under 500 µN (Fig. 2g). The uniaxial compressive strain recorded was 9.1 %. Silicon nanocolumns with diameters below 100 nm were unstable, leading to the collapse of the top SiO₂ layer (Supplementary Fig. 3a). Assuming diameters of 500–700 nm to be optimal for stability and mechanical performance in snCMUT, fabrication was equally well-defined in silicon-on-insulator (SOI) wafers with high repeatability (Supplementary Fig. 3b).

The snCMUT array was fabricated via wafer bonding of two SOI wafers using conventional microfabrication technologies (Fig. 2h, Supplementary Fig. 4). For wearable applications, PDMS was filled into trenches between elements singulated on both sides during DRIE for different trench widths to maximize flexibility (Supplementary Fig. 5).

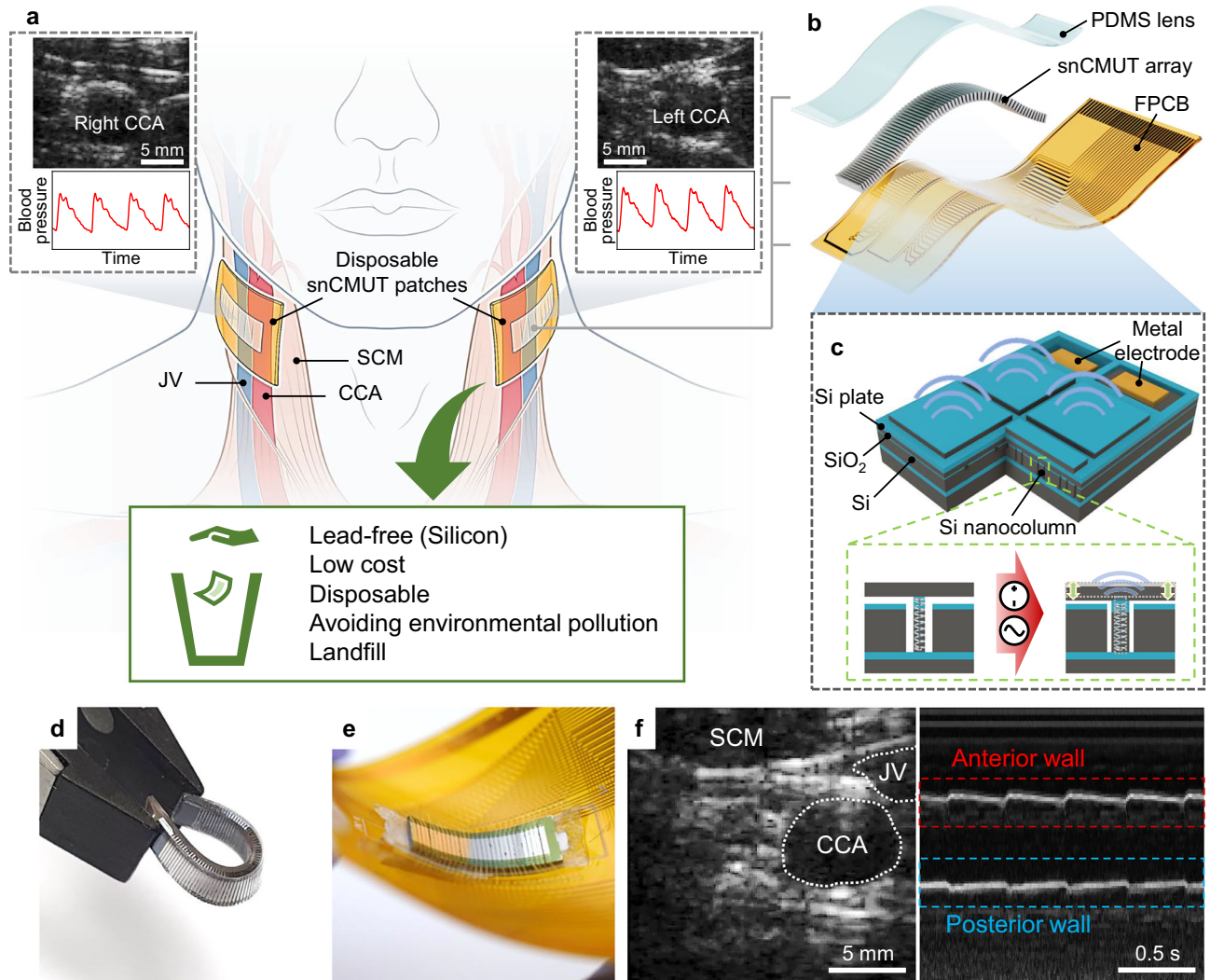


Fig. 1 | Overview of the disposable snCMUT patches. **a** Schematic illustrations of disposable snCMUT patches for continuous monitoring of both sides of the human carotid arteries. The disposable snCMUT patches are lead-free and avoid environmental restrictions. **b** Schematic illustrations of single snCMUT patch including PDMS lens, snCMUT array, and in-house designed FPCB. **c** Schematic illustrations of 4-cells of snCMUT and driving mechanism of substrate-embedded silicon

nanocolumns as springs. Optical images of the mechanical compliance of the snCMUT array when bent with a tweezer (**d**) and the disposable snCMUT patch when twisted (**e**). **f** B-mode imaging of the common carotid artery (CCA), jugular vein (JV), and sternocleidomastoid muscle (SCM) while the subject is rested (left). M-mode imaging of the pulsation pattern of CCA walls (right).

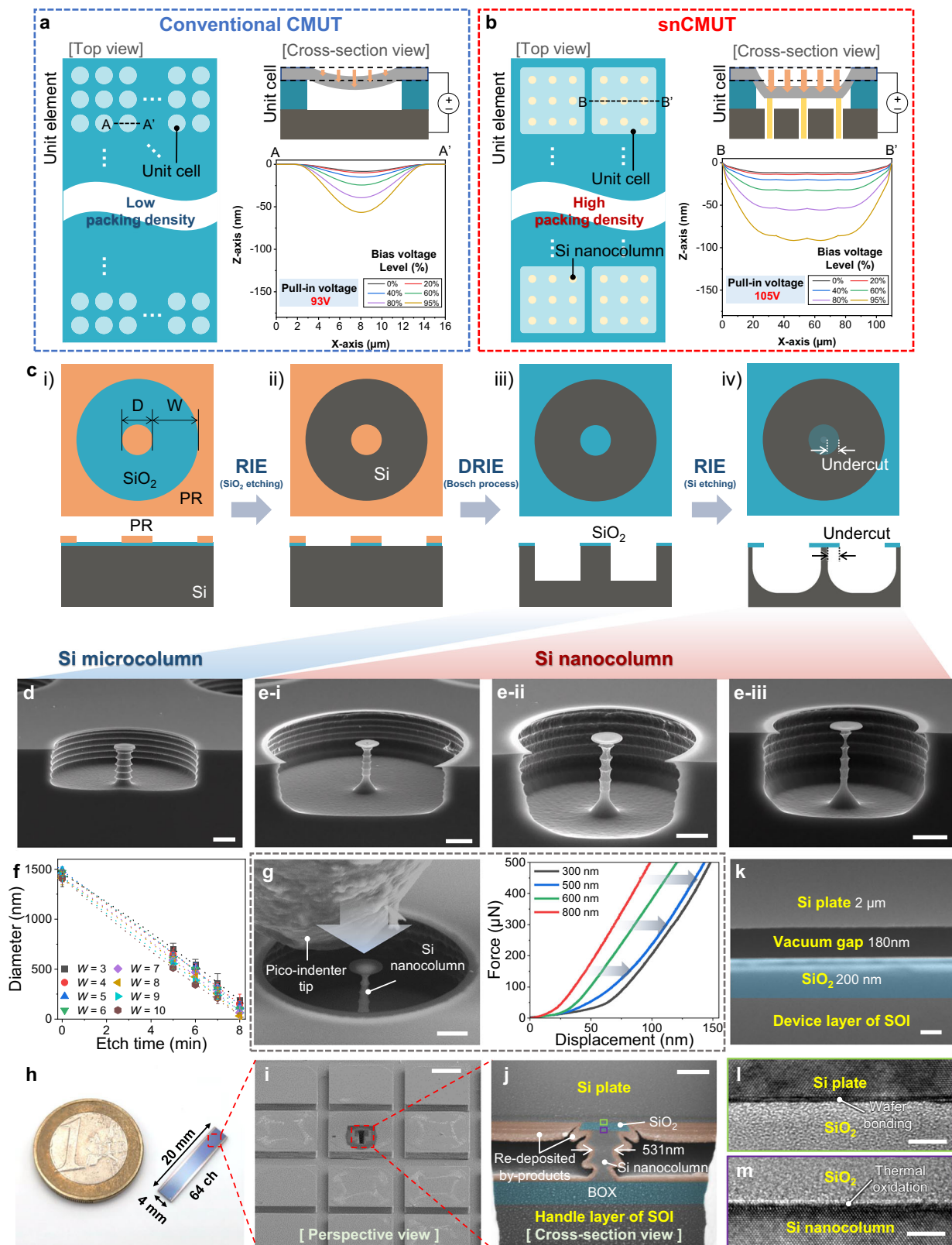
The cross-sectional cutting plane images obtained via a focused ion beam (FIB) confirmed the well-bonded silicon nanocolumns (Fig. 2i, j) and formed vacuum gaps (Fig. 2k). Transmission electron microscope (TEM) images of the wafer bonding interface (Fig. 2l) and the interface between SiO₂ grown by thermal oxidation and Si (Fig. 2m) confirmed the successful bonding of silicon nanocolumns and the Si plate of CMUT via wafer fusion bonding of two SOI wafers. The snCMUT array demonstrated impressive flexibility and stretchability, achieving bending with a radius of curvature less than 1 mm and elongation up to 140%, stretching from 40 mm to over 55 mm (Supplementary Fig. 6). The obtained high degree of stretchability prevented wearable snCMUT patch degradation, as the snCMUT array integrated into the FPCB avoided strain mismatch from tensile and compressive forces during bending.

Characterization of snCMUT

To evaluate the characteristics of the fabricated snCMUT array, a comprehensive assessment of amplitude and phase components of

the electrical input impedance was performed using an impedance analyser. Despite slight changes in the phase and amplitude of the electrical input impedance, respectively, the fabricated snCMUT exhibited sharp changes in both phase and amplitude at the resonant frequency, as analysed using DC voltage increasing from 10 to 50 V (Fig. 3a, b). Since the silicon nanocolumns functioned as springs, the shift in impedance phase with increasing bias voltage in snCMUTs was minimized compared to conventional CMUTs, which are affected by static deflections^{22,26}. An average resonant frequency of 6.7 MHz was observed in air at 50 V.

The dynamic response of the snCMUT elements was evaluated using a laser Doppler vibrometer (LDV) integrated with a custom-built microscope. With a DC bias voltage of 50 V and a continuous wave pulse of 1 VPP at 4.7 MHz, LDV recorded the piston movement of the top plate along the z-axis (Fig. 3c). Maximum displacements of 3.20 and −3.64 nm were recorded in the positive and negative z-axis directions, respectively, indicating the balanced movement of the piston top plate. The balanced movement implied well-fabricated



silicon nanocolumns and embedded snCMUTs. The peak-to-peak displacement of four-piston top plates is shown in Fig. 3d. Variations in displacement were attributed to differences in the diameter of silicon nanocolumns fabricated via the top-down approach. We suppose that precisely controlled fabrication of silicon nanocolumns would enable higher performance and be more suitable for industrial-level production (Supplementary Fig. 3c). The average volume displacement

efficiency (u_{avg}) was calculated as²²

$$u_{avg} = \frac{1}{A_{tot}} \int_{A_{tot}} u \, dA \quad (1)$$

where u denotes the corresponding displacement, and A_{tot} represents the total plate area. The average volume displacement efficiency for

Fig. 2 | Fabrication of silicon nanocolumn and snCMUT arrays. The FEA simulation of moving plate in CMUT compared to conventional CMUT (a) and snCMUT (b). The snCMUT achieves a high average displacement through the parallel motion of the plate induced by nano-silicon springs. c Schematic illustrations of fabrication steps for top-down approaches of silicon nanocolumn: i) PR patterning by conventional photolithography on a 4-inch silicon wafer after oxidation for growth silicon dioxide, ii) dry etching of silicon dioxide layer by RIE, iii) Defining silicon microcolumn via DRIE, iv) shrink down of silicon microcolumn via RIE to produce silicon nanocolumn. SEM images of fabricated silicon microcolumn (d) and silicon nanocolumns with diameters of 800 nm (e-i), 600 nm (e-ii), and 300 nm (e-iii). Etch time and opening area (W) of RIE in (e-i, ii, and iii) are 5, 6, and 8 min, 10, 5, and 4 μm , respectively. The scale bar is 2 μm . f The diameter of the silicon nanocolumn as the etch time and opening area. Data are presented as means \pm standard deviation ($n = 10$ independent samples). g SEM image of silicon nanocolumn while pico-

indentation (left) and the compressed displacement of silicon nanocolumns as pico-indentation force and diameters of silicon nanocolumns (right). The scale bar is 2 μm . h Photograph of fabricated snCMUT array. i–k SEM images of fabricated snCMUT. Perspective view of snCMUT (i). The piston top plate was cut via FIB to evaluate the dimension of the silicon nanocolumn and the vacuum gap. The cross-sectional SEM image of the silicon nanocolumn (j) and the 180 nm vacuum gap (k). During the cutting of the piston top plate via FIB, by-products from ion milling were redeposited onto the silicon nanocolumn. The scale bar is 50 μm in i, 1 μm in j, and 100 nm in (k). l, m, TEM images of wafer bonding surface (l) and thermally grown silicon dioxide surface (m). Despite the narrow cross-sectional area of the silicon nanocolumn, it was well bonded with the top SOI wafer. The scale bar is 5 nm. All the representative cross-sectional SEM and TEM images of the silicon nanocolumn were obtained from repeated experiments more than 4 times.

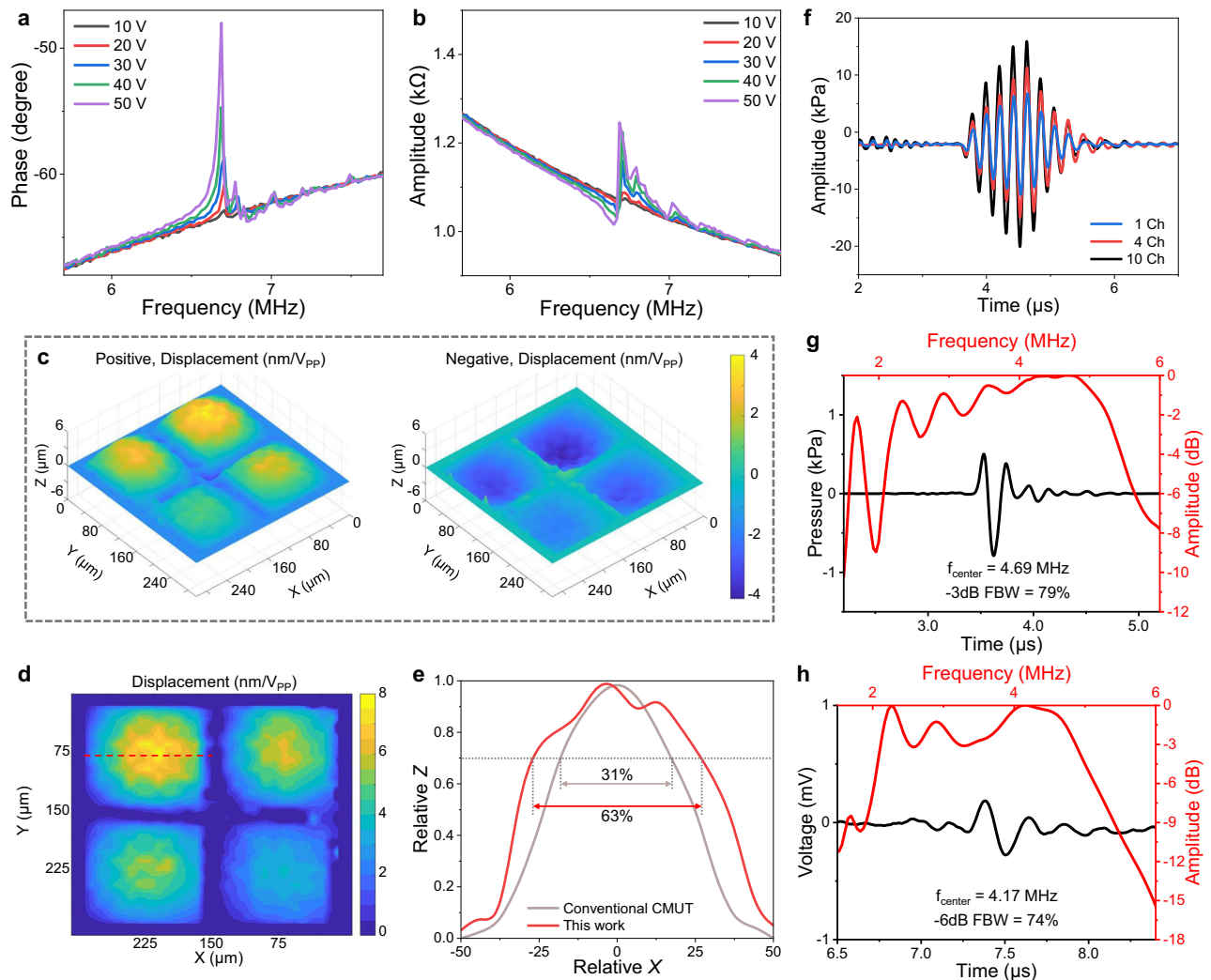


Fig. 3 | Characterization of snCMUT. Electrical impedance measurements of the corresponding element of the snCMUT: the phase part (a) and the amplitude part (b). The electrical impedance was measured using different bias voltages, 10 to 50 V of DC. Phase shifts with bias voltage were observed. The resonant frequency in air was 6.7 MHz at 50 V of bias. c The dynamic plate displacement of the snCMUT measuring from a laser Doppler vibrometer. The maximum displacement was measured in the four-piston top plate's positive (left) and negative (right) direction. d The maximum peak-to-peak displacement of the four-piston top plate. e Comparison of the displacement profile of the moving top plate between conventional CMUT and snCMUT. The measured displacement profile is from the red

dashed line in (d). The bias voltage of each CMUT is 48% of the pull-in voltage. Even though there are variations in the maximum displacement of each piston top plate, the embedded silicon nanocolumn induces parallel motion of the top plate in CMUT, which causes enhanced average displacement. f Measured acoustic pressure of the snCMUT via hydrophone as follows a number of operating elements at a distance of 3.5 mm in corn oil. g Impulse response (16.6 ns, 20V_{pp}) and its Fourier transform of a snCMUT array element under dc bias of 50 V measured by hydrophone in corn oil. h 39 dB amplified pulse-echo impulse response (16.6 ns, 20 V_{pp}) and its Fourier transform of a snCMUT array element under DC bias of 50 V reflected on ultrasound gel pad and air interface.

the four cells was 6.86, 6.84, 3.92, and 5.34 nm/V_{pp}, with a total average of 5.74 nm/V under 50 V DC bias and 1 V_{pp} AC wave, which was five times higher than those reported previously. To compare the displacement profiles of the top plate during movement in conventional CMUTs and snCMUTs, the cross-sectional profile of snCMUT was used (Fig. 3e). After normalising the cell dimensions and maximum displacement, the areas with 70% maximum displacement comprised 31% conventional CMUTs and 63% snCMUTs. Thus, snCMUTs generated top-plate movement over a broader area, resulting in higher average displacement efficiency and consequent greater transmission efficiency.

The maximum output pressure and transmission efficiency of snCMUT were evaluated using a hydrophone in corn oil. The hydrophone with a pre-amplifier and oscilloscope monitored the pressure field of 3.5 mm away from the snCMUT elements with a DC bias voltage of 50 V and a 5 V_{pp} AC wave at 4.65 MHz. Transient pressure amplitudes of 16.7, 27.5, and 37.5 kPa for 1, 4, and 10 channels, respectively, are shown in Fig. 3f. The calculated maximum transient pressure at the surface was 1.51 MPa peak-to-peak, achieved with 5-cycle pulses at 4.65 MHz and 5 V_{pp}. Approximately five cycles were necessary to transition from the asymmetric motion of the piston top plate, caused by the varying spring constants of individual silicon nanocolumns due to fabrication-related variances, to a symmetric motion influenced by the weight of the piston top plate (Supplementary Fig. 7). Herein, snCMUT exhibited a −3 dB fractional bandwidth (FBW) of 79% at 4.69 MHz, which was lower than that of conventional CMUTs due to silicon nanocolumn fabrication variations and the weight of the piston top plate (Fig. 3g). However, the −6 dB FBW of the frequency spectrum and the resonance frequency in pulse-echo response slightly narrowed to 74% at reduced resonance frequency of 4.17 MHz due to the encapsulation layers of parylene-c and PDMS that attributes as an loading mass in spring-mass-damper system (Fig. 3h). Higher FBW could be achieved by reducing variations in dimension of silicon nanocolumns using advanced lithography techniques and optimized packaging.

Comparative analyses of snCMUT with commercial lead zirconate titanate (PZT) probes, conventional CMUT, and enhanced CMUT (Supplementary Table 3) were conducted. Maximum pressure at the transducer surface was calculated to mitigate the impact of varying aperture sizes and focal lengths, accounting for acoustic attenuation and lens-induced gain. Commercial PZT transducers and conventional CMUT exhibited transmission efficiencies of 13.4 and 6.30 kPa/V, respectively^{22,28}. Previous efforts improved CMUT transmission efficiency to 21.5 kPa/V using post-CMUTs²² and 61.2 kPa/V using electro-deposit CMUTs (EP-CMUT)²³. Herein, snCMUT achieved a transmission efficiency of 220 kPa/V, a tenfold increase over post-CMUT and 3.6-fold over EP-CMUT. The parallel movement of the piston top-plate facilitated by silicon nanocolumns boosted the efficiency, enhancing volume displacement and transmission efficiencies with low voltage requirements. Thus, the proposed ultrasound transducers were proven to be highly suitable for wearable ultrasound technologies, offering high performance, low energy consumption, environmental adaptability, and disposability.

Comparative study on the ultrasound imaging performance of snCMUT on phantom

Conventional CMUTs directly connected to imaging systems generally suffer from degraded SNR due to large capacitances in flexible cables (hundreds of pF)^{29–31}. To mitigate this issue, conventional CMUTs typically use application-specific integrated circuits (ASICs) placed close to the CMUT to improve SNR^{29–31}. However, ASICs are expensive and present a significant challenge in developing wearable and disposable ultrasound patches.

In contrast, snCMUT achieved sufficient SNR through its high transmission efficiency, eliminating the requirement for ASICs. Thus,

system complexity and cost were reduced, along with lower power consumption, making snCMUT advantageous for use in wearable and disposable ultrasound patches. The fabricated disposable snCMUT patches included a custom-made FPCB directly connected to the Vantage 256 research ultrasound system, enabling simultaneous non-invasive monitoring of multiple body locations. The packaged patch was thin (933 μm, Supplementary Fig. 8) and suitable for attachment to the human body (Fig. 1f). An in-house imaging code was developed to reconstruct the acquired images. To correct positional changes of each element in the wearable ultrasound patch in real-time, a technique from a previously published patent was used to detect relative positions by measuring capacitance changes between each singulated CMUT element (Supplementary Fig. 9). Image reconstruction was performed using a plane-wave compounding algorithm with 57 angles (Supplementary Fig. 10).

To evaluate the wearable ultrasound imaging capabilities of the snCMUT patches, a multi-purpose ultrasound phantom (model ATS-539, CIRS) was used, combining monofilament line targets for distance measurements and tissue-mimicking target structures of varying sizes and contrasts (Supplementary Fig. 11a). For a comparative illustration of resolution between the disposable snCMUT patch and a conventional CMUT probe, images were captured in real-time up to a depth of 90 mm (Fig. 4a, b). The conventional CMUT fabricated via the wafer bonding method in the same manner as snCMUT but exhibited insufficient imaging performance under identical operating conditions to the snCMUT (Supplementary Fig. 11b). Therefore, the conventional CMUT was optimized for imaging by adjusting the DC bias voltage and AC voltage frequencies, operating at 70 V and 30.6 V_{pp} at 6.25 MHz, respectively. The ultrasound images from the conventional CMUT showed axial-lateral resolution and anechoic targets up to a depth of 40 and 20 mm, respectively (Fig. 4c, Supplementary Fig. 11c). The disposable snCMUT patch operated at a lower voltage compared to the conventional CMUT (DC bias voltage of 40 V and AC voltage of 8.9 V_{pp} at 4.25 MHz). After packaging, the resonant frequency shifted from 4.65 to 4.25 MHz due to the damping effect of the PDMS lens covering the piston top plate. Ultrasound images from the snCMUT patches demonstrated the ability to resolve axial-lateral resolution targets at depths of approximately 75 mm, even at low voltages (Fig. 4d, e, Supplementary Fig. 11d). The anechoic target structure was distinguishable up to a depth of 30 mm.

While analyzing ultrasound image intensity in the axial direction, the conventional CMUT showed the lowest background noise of −18 mm and failed to distinguish the wire target beyond 40 mm. Conversely, the disposable snCMUT patch exhibited the lowest background noise at −40 mm and produced distinguishable images up to 70 mm (Fig. 4f). The disposable snCMUT patch achieved notable axial and lateral resolutions of 0.52 and 0.55 mm, respectively, in a 100 μm nylon monofilament phantom. Both the conventional CMUT probe and the disposable snCMUT patch demonstrated excellent axial and lateral resolutions below 1 mm compared to the commercial PZT-based probe. However, due to lower transmission efficiency, the conventional CMUT experienced a blurred image beyond 40 mm, while the snCMUT patch maintained sub-1 mm resolutions up to 70 mm (Fig. 4g, h). Furthermore, the snCMUT patch displayed higher ultrasound image contrast than the conventional CMUT probe, attributed to its superior SNR resulting from higher transmission efficiency (Fig. 4i).

The superior performance of the disposable snCMUT patch was established by comparing it with previously reported wearable ultrasound probes (Supplementary Table 2). Recently published wearable ultrasound probes have achieved high frequencies and relatively high axial and lateral resolution in rigid forms, but their thickness exceeds 3 mm, limiting their applicability in wearable devices¹⁴. Stretchable ultrasound probes, while relatively thin at 1 mm, suffer from poor lateral resolution of 2 mm due to wide pitch and kerf^{4,13}. Probes using

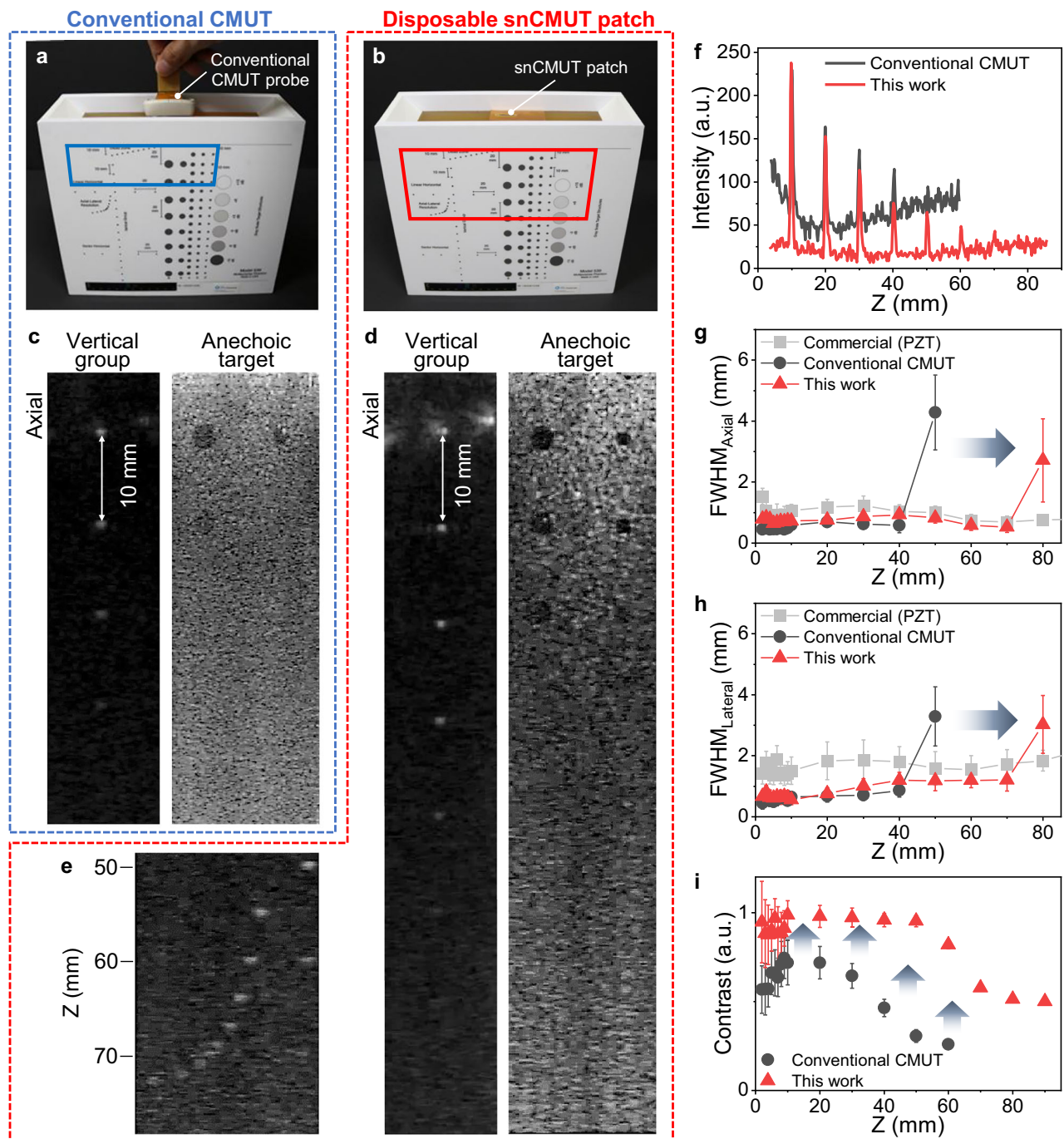


Fig. 4 | Ultrasound images of the commercial phantom and their evaluation. The optical photograph of the conventional CMUT probe (**a**) and the disposable snCMUT patch (**b**) on the top surface of the commercial phantom with ultrasound gel. The blue and red boxes indicate the visible area of the phantom by conventional CMUT and disposable snCMUT patches, respectively. **c** B-mode images of the conventional CMUT probe in the vertical group and anechoic target of the commercial phantom. The conventional CMUT was operated with a DC bias voltage of 70 V, complemented by 30.6 V_{pp} and 6.25 MHz of AC wave. B-mode images of the disposable snCMUT patch in the vertical group and anechoic target (**d**) and the axial-lateral resolution array (**e**) of the commercial phantom. The snCMUT was operated with a DC bias voltage of 40 V, complemented by 8.9 V_{pp} and 4.25 MHz of

AC wave. **f**, Intensity of vertical group targets as a function of the imaging depth of conventional CMUT and snCMUT. All values are expressed in a.u., which denotes arbitrary units. Axial (**g**) and lateral (**h**) resolutions of the vertical group targets along the imaging depth compared between PZT-based commercial ultrasound probe, conventional CMUT, and snCMUT. Data are presented as means \pm standard deviation ($n = 4$ independent experiments). **i** Contrast of B-mode images as a function of the imaging depth of conventional CMUT and snCMUT. Compared to the conventional CMUT probe, the disposable snCMUT patch offers enhanced contrast and the ability to image deeper regions, thanks to its high transmission efficiency. Data are presented as means \pm standard deviation ($n = 4$ independent experiments). All values are expressed in a.u., which denotes arbitrary units.

PVDF are highly thin (0.1 mm) and flexible, but they require a high working voltage (95 V_{pp}), trans-impedance amplifiers, and digitized amplification⁶. Contrarily, the disposable snCMUT patch is stretchable (excluding the FPCB) and fully packaged at less than 1 mm thickness.

The disposable snCMUT patch achieved very high imaging quality, with axial and lateral resolutions of less than 0.55 mm, even at a very low working voltage of 8.9 V_{pp}, owing to its high transmission efficiency and no requirements for ASICs to improve SNR.

Real-time imaging and blood pressure waveform monitoring from carotid artery

After evaluating and optimizing ultrasound images of the disposable snCMUT patches using a commercial multi-purpose phantom, the patches were applied to perform real-time monitoring of the carotid artery in the human neck (Fig. 5a). Cardiovascular diseases, including heart conditions such as arrhythmia and vascular issues from cholesterol buildup, can disrupt blood flow in the carotid artery, leading to strokes^{32,33}. Continuous monitoring of the artery is crucial for preventing such events. Wearable ultrasound patches offer continuous, non-invasive monitoring of arterial health, providing critical insights into cardiovascular status^{33,34}. They improve patient compliance by eliminating the discomfort of traditional methods and enhance medication adherence through real-time feedback. Monitoring both carotid arteries is advantageous, as it helps detect asymmetrical arterial stiffness and localized issues such as atherosclerosis, offering a more comprehensive assessment of cardiovascular health^{24,25}. Furthermore, bilateral monitoring is used to identify significant blood pressure differences between the arteries, indicating severe conditions such as stenosis or aortic dissection²⁵. This approach enhances patient safety and supports better treatment planning and postoperative care, particularly in high-risk patients and those undergoing carotid artery surgery.

Two disposable snCMUT patches were conformally placed in contact on both sides of the necks of 9 healthy volunteers for simultaneous monitoring of the left and right carotid arteries (Supplementary Fig. 12). To locate the carotid artery, the disposable snCMUT patch was moved while observing and acquiring B-mode images (Supplementary videos 1 and 2). For the safety of the subjects, the bias voltage was limited to 30 V. The disposable snCMUT patches were operated under 24.5 V_{pp} of 4.25 MHz pulse. The vertical cross-sections of the common carotid artery (CCA) on the right (Fig. 5b) and left (Fig. 5c) sides of the neck were monitored via B-mode ultrasound images. The enhanced transmission efficiency provided by silicon nanocolumns allowed for relatively clear ultrasound images compared to previously reported wearable ultrasound imagers^{4,8}, enabling the distinction of CCA and the internal jugular vein (JV) and sternocleidomastoid muscle (SCM). In the transverse ultrasound images of the carotid artery, the outer wall of the CCA was relatively clearly identified (Fig. 5d), and pulsations were monitored in real-time. Despite operating at a very low voltage, the disposable snCMUT patches obtained more precise ultrasound images than previously reported wearable ultrasound imagers that required voltage amplification up to 200 V by boost converters with high power consumption. The low operating voltage was remarkable and required for wearable ultrasound patches.

The blood pressure of the carotid artery acquired from the disposable snCMUT patches attached to the human neck through M-mode ultrasound imaging allowed continuous monitoring of the pathophysiological status (Fig. 5e). The contraction and expansion of the carotid artery were measured through the positional changes of the anterior and posterior walls, tracking the blood pressure changes over time. The changes in the distance between carotid artery walls were converted into blood pressure pulse waves and compared with a clinical-grade tonometer. The disposable snCMUT patch exhibited over 96.5% agreement with the clinical-grade tonometer (Fig. 5f, Supplementary Fig. 13), even preventing potential operator-dependent recording errors using handheld probes, such as vessel squeezing or misalignment (Supplementary Fig. 14). In healthy volunteers, there was little difference in blood pressure readings obtained simultaneously from both sides of the neck using the disposable snCMUT patches (Fig. 5g), as healthy individuals typically do not exhibit carotid artery asymmetry. Continuous monitoring of the carotid arteries in patients using disposable snCMUT patches can help detect asymmetrical arterial stiffness and localized conditions such as atherosclerosis, offering a more comprehensive assessment of cardiovascular health.

For this study, the human carotid artery was continuously monitored using low-cost, ultra-thin, silicon-based disposable snCMUT, obtaining detailed blood pressure pulse waveforms, including the maximal slope, systolic peak, dicrotic notch, and diastolic peak.

In conclusion, developing disposable snCMUT patches marks a significant advancement in wearable ultrasound technology. The proposed patches offer a lead-free, flexible, and cost-effective solution for real-time medical imaging and monitoring. Using semiconductor fabrication on silicon wafers, snCMUTs present an eco-friendly alternative to traditional lead-based piezoelectric materials, significantly reducing manufacturing costs and making disposable probes a viable option. By incorporating silicon nanocolumns, the patches deliver high transmission efficiency and superior image resolution at low operational voltages, making them ideal for continuously monitoring critical parameters such as blood pressure and arterial health. Exceptional flexibility and thinness make snCMUT patches particularly suited for wearable applications, while their enhanced imaging performance and improved SNR have been validated in both phantom imaging and real-time carotid artery monitoring on both sides of the neck simultaneously. The innovation offers a promising approach to non-invasive cardiovascular health monitoring, providing valuable clinical insights with minimal discomfort and high diagnostic accuracy. Further integration with ASIC-based electronics and wireless modules could enable fully integrated, stand-alone wearable ultrasound systems in future developments. Currently, the application of the low-cost, disposable snCMUT patches across various parts of the human body is under development to capture real-time three-dimensional ultrasound images, which is expected to enhance ultrasound imaging further and deliver crucial clinical insights.

Methods

Ethics approval and participant information

All research involving human participants was conducted in accordance with relevant ethical regulations and approved by the Institutional Review Board of Seoul National University Hospital (IRB No. H-2007-145-1143). Ten healthy adult volunteers were initially recruited regardless of sex or gender. Of these, nine participants completed the study. All participants provided written informed consent prior to participation. Sex and gender were not considered in the study design, as the objective was to evaluate the technical performance of the ultrasound patch, independent of sex-based physiological factors. No sex- or gender-based subgroup analysis was conducted.

Materials

All chemicals used during the fabrication of CMUT, including acetone, isopropyl alcohol (IPA), buffered oxide etchant (BOE) 6:1, hydrogen peroxide, and sulfuric acid, were purchased from Daejung Chemicals, Inc. (South Korea). Highly doped silicon wafers (p-type, 100) were purchased from WaferBiz (South Korea). On the other hand, highly doped SOI wafers (p-type, 100) were purchased from BMIT (South Korea). In conventional photolithography, two photoresist (PR) types were used: positive and negative PR. The positive PRs used were AZ GXR-601 (46 cP) and AZ 10-XT (520 cP) from Merk KGaA (Germany). The negative PRs, namely DNR-L-300-40 (120 cP) and DNR-L-300-D1 (21.8 cP), were purchased from Dongjin Semichem Co., Ltd. (South Korea). Aluminium etchant APAL-1 was purchased from Labotech (South Korea). Polydimethylsiloxane (PDMS; SYLGARD 160) for the acoustic lens was purchased from Dow Corning (USA).

Fabrication of silicon nanocolumns

Four-inch bare silicon and SOI wafers were used to establish top-down fabrication of silicon nanocolumns at a single wafer level. The silicon and SOI wafers underwent a thermal treatment in an 1100 °C furnace, resulting in the growth of a 200 nm silicon dioxide layer. Negative PR was applied to define silicon columns using conventional

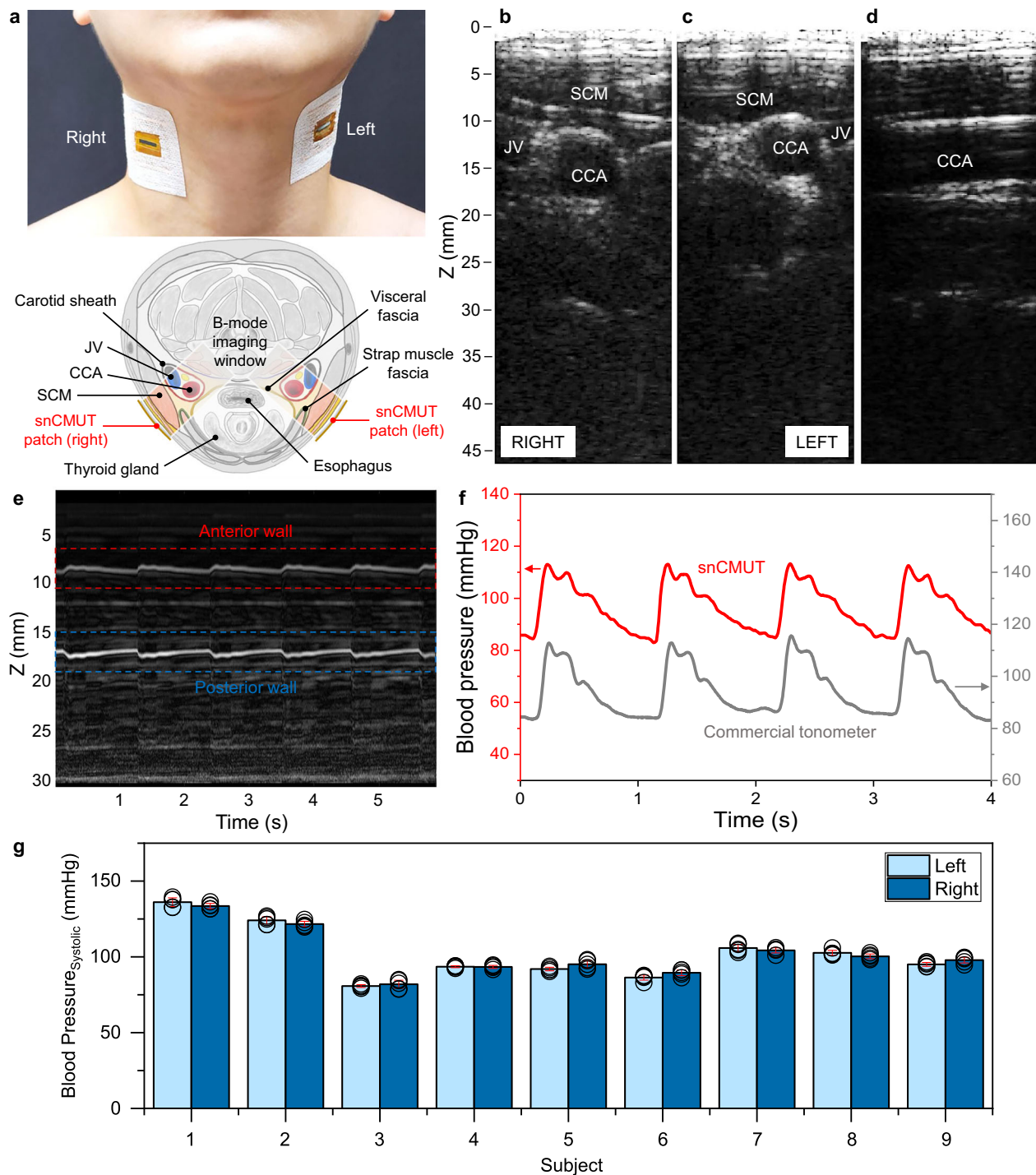


Fig. 5 | Human carotid artery ultrasound images and monitoring of blood pressure obtained with prototype disposable ultrasound patches.

a Photograph of attached disposable snCMUT patches onto both sides of the human neck for real-time ultrasound imaging and blood pressure monitoring of human carotid arteries. The B-mode images at the human neck surface aligned with vertical cross-sections of the common carotid artery (CCA) on the right (**b**) and left (**c**) side of the neck. The enhanced transmission efficiency provided clear ultrasound images, enabling the distinction of not only the CCA but also the internal jugular vein (JV) and sternocleidomastoid muscle (SCM). **d** The B-mode image of left neck side transverse CCA for monitoring carotid artery pulsations from

detecting wall. The applied DC bias voltage was 30 V supplemented by 24.5 V_{pp} of 4.25 MHz AC wave for ultrasound imaging via disposable snCMUT patches.

e M-mode image of the pulsation pattern of CCA walls. **f** The waveforms of blood pressure derived from carotid vessel diameters of the M-mode image (**e**) as a function of time. Physiological parameters from the arterial pulse waveforms, including the heart rate and blood pressure, were derived. **g** Systolic blood pressure on the left and right side of the neck of 9 healthy volunteers simultaneously monitored by two disposable snCMUT patches. Data are presented as means \pm standard deviation ($n = 5$ independent experiments).

photolithography. Specifically, DNR-L300-D1 (21.8 cP) was spin-coated on the wafer. Following a baking step, UV light was exposed to the substrate using an EVG®6200 NT mask aligner (EV Group, Austria), and subsequent pre-exposure bake and development (AZ 300 MIF) processes were conducted. Furthermore, the silicon dioxide layer was etched using RIE via Plasmalab800Plus (Oxford Instruments, UK). DRIE was employed to define silicon columns at the micrometre scale using the Omega® LPX-DSi Etch system (SPTS Technologies Ltd., United Kingdom). A second round of RIE was applied to the micro-silicon columns to reduce their size through undercutting via horizontal etching, which smoothed the scallops from DRIE. Additionally, a systematic investigation was conducted on the anisotropy of the RIE process, and the etching conditions were fine-tuned to achieve precise fabrication of nano-sized silicon columns as springs.

Evaluation of mechanical characteristics of silicon nanocolumns

To evaluate the top-down fabricated silicon nanocolumns, in-situ nanomechanical characterizations were performed using a pico-indenter (Hysitron PI 85 L PicoIndenter; Bruker, Corp., USA), which was integrated with the imaging capabilities of a scanning electron microscope (SEM) (Nova Nano SEM 450; FEI, Netherlands), allowing for simultaneous quantitative nanomechanical testing and imaging. A 10 µm diameter flat tip was employed to apply force to the nanocolumns, facilitating the assessment of their elastic deformation. To minimize buckling, the flat tip was positioned as perpendicular to the substrate as possible. For accurate characterization, the silicon nanocolumns were subjected to repeated compression by the pico-indenter across at least 10 individual samples, and the average displacement was recorded.

Design and fabrication of snCMUT array

To integrate silicon nanocolumns into CMUT as springs, FEA was conducted using the commercial tool COMSOL Multiphysics (COMSOL, Inc., USA). Nine silicon nanocolumns were arranged in a 3 × 3 grid within a single cell of the CMUT, and each cell was designed as a square with dimensions of 120 × 120 µm. A vacuum gap of 180 nm was designed for ultrasound generation. A single element in the CMUT array comprised 40 cells arranged in a 2-row and 20-column configuration. A piston structure (stiff block) was positioned above each cell to prevent the bending of the moving plate. The thickness of the moving plate was set at 2 µm, and the 64-element CMUT array was designed with a resonance frequency of 5 MHz for ultrasound imaging of the human carotid artery vessels.

The fabrication involved wafer bonding of two SOI wafers, which had undergone DRIE and chemical mechanical polishing (CMP) to ensure precise dimensional control during fabrication. A SOI wafer with a device layer electrical resistivity of <0.005 ohm-cm was selected to establish bottom and top plate electrodes.

Fabrication details are provided in Supplementary Fig. 4. Initially, a silicon dioxide layer was grown and patterned on the SOI wafer using conventional photolithography techniques (EVG®6200 NT mask aligner, EV Group, Austria). Subsequent oxidation resulted in a vacuum gap height of 180 nm. The CMUT element and the lateral dimensions of the silicon nanocolumns were defined through DRIE using the Omega® LPX-DSi Etch system (SPTS Technologies Ltd., United Kingdom) after the silicon dioxide layer was etched using RIE via Plasmalab800Plus (Oxford Instruments, UK). The top-side SOI wafer was roughly aligned with the processed bottom SOI wafer, and wafer bonding was accomplished in a high-vacuum environment using the SB8 GEN2 system (Suss Microtec, Germany). The handle layer of the top SOI wafer was then grounded and polished to obtain 20 µm-thick piston top plates. A silicon dioxide mask was grown, accurately defining the piston structures and defining the top plate using DRIE. To establish electrical contact for the bottom and top plate electrodes, the layers including the buried oxide (BOX) layer, the device layer of

the top SOI wafer, and the silicon dioxide layer in the bottom SOI wafer, were sequentially etched. The process culminated with the deposition and patterning of a 500 nm aluminum layer to create electrical contact pads. Each CMUT element was singulated via front-side and backside trenches formed by conventional photolithography and DRIE. The trenches were filled with PDMS to produce flexible and stretchable snCMUTs. Following fabrication, the processed SOI wafer was diced via blade dicing to segment the arrays of snCMUTs.

Characterization of snCMUT array

For evaluating the fabricated snCMUT array, SEM examinations were conducted using the Nova Nano SEM 450 (FEI, Netherlands). To carefully assess the shape of the silicon nanocolumns within the snCMUTs, focused ion beam (FIB) cutting was employed using NX 5000 (Hitachi, Japan). This process enabled precise vertical sectioning of the silicon nanocolumns, facilitating SEM observations to measure their shapes and dimensions. Additionally, the establishment of the vacuum gap and bonding of the moving plate were verified.

To delve into the operational characteristics of the fabricated snCMUTs, an impedance analyser (4294 A, Agilent Technologies Inc., USA) was used to confirm the phase and amplitude of the electrical input impedance, thereby assessing the electrical properties. A DC bias was applied to the snCMUT array via a bias T circuit and a high-voltage power supply, with a small-signal AC voltage of 100 mV superimposed (Supplementary Fig. 15). Calibration was meticulously conducted to invalidate potential parasitic influences. To analyze the mechanical movement of the moving plate of snCMUTs, an LDV integrated with a microscope (OFV-2570; Polytec GmbH, Germany) was employed (Supplementary Fig. 16). Measurement of the acoustic pressure generated by the snCMUT was conducted using a hydrophone (HNR-0500; Onda Co., USA) coupled with a pre-amplifier (Supplementary Fig. 17). The hydrophone signals were read out through a digitizing oscilloscope (Infiniium 54825 A; Agilent Technologies Inc., USA). To simultaneously apply DC and AC voltages, a bias T circuit was used, with the DC voltage sourced from a high-voltage power supply (SRS PS310; Stanford Research System, USA) and the AC voltage with broadband excitation of 16.6 ns impulse signal (20 V) applied through the AC function generator (Agilent 33500B; Agilent Technologies Inc., USA) to snCMUT array for FBW analysis. The input impulse signal spectrum and the hydrophone sensitivity spectrum normalization were conducted on the transmitted ultrasound pressure spectrum for precise analysis of FBW. Similarly, the FBW of the pulse-echo signal from snCMUT, reflected on ultrasound gel pad (WATER GEL; BLUE-MTECH, Korea) and air interface, was calculated by acquiring signals using the oscilloscope.

Packaging and prototyping disposable snCMUT patch

To produce snCMUT for disposable patches, an in-house-designed FPCB was fabricated and employed. An adhesive was used to demonstrate the wearable CMUT's capability for ultrasound imaging to mount the fabricated snCMUT array. The FPCB was designed to include connectors for a commercial ultrasound imaging system (Vantage 256 research ultrasound system; Verasonics Inc., USA). Pre-tests were conducted using wire-bonding and anisotropic conductive film (ACF) for the electrical connection between snCMUT and FPCB. Since no significant differences were observed between the two methods, both methods were used for packaging. After electrical connections, 100 nm of parylene C was deposited via a parylene coating system (LAVIDA 110; FemtoScience, South Korea). The entire assembly was encapsulated with a PDMS lens for insulation and ultrasound focusing.

Acoustic characterizations using commercial standard phantom

In this study, the conventional CMUT probe selected for comparison with snCMUT was fabricated using double oxidation and standard

wafer bonding process^{35–37}, comprising a 192 channels linear array. Only 64 channels were operated for acoustic characterizations, the same as the number of channels in the snCMUT array. Imaging performance evaluation of both conventional CMUT probe and disposable snCMUT patch was conducted using standard ultrasound imaging phantom (ATS-539, CIRS) for dead zone group (2–10 mm, with 1 mm spacing), vertical group (10–180 mm, with 10 mm spacing), axial-lateral resolution array (40, 70, 110, and 160 mm, with 4, 3, 2, 1, 0.5, and 0.25 mm spacing) and anechoic target structures (10–170 mm, with 20 mm spacing). Transducers were vertically placed on the surface of the phantom using ultrasound gel and operated using a commercial ultrasound imaging system (Vantage 256 system, Verasonics, Inc.) to scan over the phantom and reconstruct the imaging planes by employing a plane-wave compounding method, custom-programmed by MATLAB (MathWorks). Pulse-echo intensity, axial/lateral full width half maximum (FWHM) based on the point spread function (PSF) of the target, and ultrasound image contrast were analysed from the ultrasound images of the phantom targets acquired by both the conventional CMUT probe and disposable snCMUT patch.

Wearable B-mode imaging on the human body

The bio-interface excursions, carotid artery, and blood pressure waveforms were measured in healthy participants (Supplementary Fig. 18a). All human tests were approved by the Seoul National University College of Medicine and Seoul National University Hospital, Institutional Review Board protocol (H-2007-145-1143). The participants provided their voluntary consent for ultrasonic measurements.

Using the disposable snCMUT patches, real-time B-mode imaging on the human body was performed on nine healthy participants with relatively low and stable bias voltage for CMUT (30 V) provided by a commercial DC supply (PS310, Stanford Research Systems) and a transmitting voltage (24.5 V_{pp}) provided by a commercial multi-channel controller, which was within the safe range of intensity defined by the Food and Drug Administration (<190 W/cm²) to ensure the safety of the subject.

Disposable snCMUT patches were attached to the skin surface using commercial medical tape (3 M Soft Cloth Tape with Liner 2762, 3 M Company), manually aligned to the cross-sectional area of the CCA through real-time B-mode imaging. To minimize motion artifacts during measurements, we instructed the participants to maintain a stable posture throughout the procedure. High-quality images of the CCA and adjacent JV and SCM were acquired using disposable snCMUT patches operated by the commercial multi-channel controller with a custom-programmed plane-wave compounding reconstruction algorithm. To enable real-time monitoring of both carotid arteries, two synchronized commercial ultrasound imaging systems (Vantage 64 and Vantage 256, Verasonics, Inc., USA) were utilized. These systems were programmed using MATLAB R2022a (MathWorks, Inc., USA) and interfaced with host PCs via Peripheral Component Interconnect Express (PCIe). A 30 V DC bias voltage, supplied by a DC power supply, was applied through a bias T to the driving signals for snCMUT patch operation. The reflected ultrasound signals were received and processed within the Vantage systems, enabling real-time bilateral carotid artery imaging (Supplementary Fig. 18b).

Measurement and validation of blood pressure waveforms on carotid artery

Based on the real-time B-mode imaging acquired by the disposable snCMUT patch, a single channel of the patch facing the top surface of the anterior wall of the CCA was manually selected for operation using M-mode imaging, specifically for measuring the CCA blood vessel diameter change over time acquired from pulse-echo signals from the anterior and posterior walls of the CCA. Using the established analytical model based on arterial wall deformation presented by Wang et al.³⁸, blood vessel diameter information was acquired and filtered to

calculate the blood pressure waveforms (p(t)) of CCA.

$$p(t) = p_d * e^{\alpha \left(\frac{A(t)}{A_d} - 1 \right)} \quad (2)$$

Here, p_d and p_s represent diastolic and systolic pressures, respectively, which were calibrated using standard values obtained from a commercial blood pressure cuff (as described in the Supplementary Information). A_d is the diastolic arterial cross-sectional area, and the time-dependent arterial cross-sectional area, $A(t)$, and the rigidity coefficient α is given by:

$$A(t) = \frac{\pi d^2(t)}{4}, \alpha = \frac{A_d \ln \left(\frac{p_s}{p_d} \right)}{A_s - A_d} \quad (3)$$

To validate the ability of the disposable snCMUT patches to measure blood pressure waveforms, the commercial pressure sensor-based blood pressure waveform analyser (DMP-1000 PLUS, DAEYO-MEDI Co., Ltd., South Korea) was used to acquire blood pressure waveforms of CCA at the exact position of the same subject in close succession after the measurement using the disposable snCMUT patch. Systolic and diastolic blood pressure values from a commercial blood pressure cuff (JPN616T, OMRON Corporation, Japan) were additionally provided for calculating actual blood pressure for both disposable snCMUT patch and commercial pressure sensor.

Reporting summary

Further information on research design is available in the Nature Portfolio Reporting Summary linked to this article.

Data availability

All data supporting the findings and conclusions of this study are available within the paper and its Supplementary Information files. All other relevant data are available from the corresponding author upon request. Source data are provided in this paper. Source data are provided with this paper.

Code availability

Codes used to post-process the ultrasound data within this paper are available from the corresponding author upon request.

References

- La, T. & Le, L. H. Flexible and wearable ultrasound device for medical applications: a review on materials, structural designs, and current challenges. *Adv. Mater. Technol.* **7**, 2100798 (2022).
- Brenner, K. et al. Advances in capacitive micromachined ultrasonic transducers. *Micromachines* **10**, 152 (2019).
- Khuri-Yakub, B. T. & Oralkan, Ö. Capacitive micromachined ultrasonic transducers for medical imaging and therapy. *J. Micromech. Microeng.* **21**, 054004 (2011).
- Hu, H. et al. A wearable cardiac ultrasound imager. *Nature* **613**, 667–675 (2023).
- Christensen-Jeffries, K. et al. Super-resolution ultrasound imaging. *Ultrasound Med. Biol.* **46**, 865–891 (2020).
- van Neer, P. L. M. J. et al. Flexible large-area ultrasound arrays for medical applications made using embossed polymer structures. *Nat. Commun.* **15**, 2802 (2024).
- Lin, M., Hu, H., Zhou, S. & Xu, S. Soft wearable devices for deep-tissue sensing. *Nat. Rev. Mater.* **7**, 850–869 (2022).
- Lin, M. et al. A fully integrated wearable ultrasound system to monitor deep tissues in moving subjects. *Nat. Biotechnol.* **42**, 448–457 (2024).
- Zhang, L. et al. A conformable phased-array ultrasound patch for bladder volume monitoring. *Nat. Electron* **7**, 77–90 (2023).
- Liu, H.-C. et al. Wearable bioadhesive ultrasound shear wave elastography. *Sci. Adv.* **10**, eadk8426 (2024).
- Li, Y. et al. Progress in wearable acoustical sensors for diagnostic applications. *Biosens. Bioelectron.* **237**, 115509 (2023).

12. Hu, H. et al. Stretchable ultrasonic arrays for the three-dimensional mapping of the modulus of deep tissue. *Nat. Biomed. Eng.* 1–14 <https://doi.org/10.1038/s41551-023-01038-w> (2023).
13. Wang, C. et al. Continuous monitoring of deep-tissue haemodynamics with stretchable ultrasonic phased arrays. *Nat. Biomed. Eng.* **5**, 749–758 (2021).
14. Wang, C. et al. Bioadhesive ultrasound for long-term continuous imaging of diverse organs. *Science* **377**, 517–523 (2022).
15. Hu, H. et al. Stretchable ultrasonic transducer arrays for three-dimensional imaging on complex surfaces. *Sci. Adv.* **4**, eaar3979 (2018).
16. Wygant, I. A comparison of CMUTs and piezoelectric transducer elements for 2D medical imaging based on conventional simulation models. in *2011 IEEE International Ultrasonics Symposium* 100–103 (IEEE, 2011).
17. Panda, P. K., Sahoo, B., Thejas, T. S. & Krishna, M. High d33 lead-free piezoceramics: a review. *J. Electron Mater.* **51**, 938–952 (2022).
18. Waqar, M., Wu, H., Chen, J., Yao, K. & Wang, J. Evolution from lead-based to lead-free piezoelectrics: engineering of lattices, domains, boundaries, and defects leading to giant response. *Adv. Mater.* **34**, 2106845 (2022).
19. Erguri, A. S. et al. Capacitive micromachined ultrasonic transducers: fabrication technology. *IEEE Trans. Ultrason Ferroelectr. Freq. Control* **52**, 2242–2258 (2005).
20. Fraser, J. D. Capacitive micromachined ultrasonic transducers. *J. Acoust. Soc. Am.* **113**, 1194 (2003).
21. Bhatti, M. T. et al. Thermal analysis and SNR comparison of CMUT and PZT transducers using coded excitation. *Ultrasonics* **136**, 107148 (2024).
22. Lee, B. C., Nikoozadeh, A., Park, K. K. & Khuri-Yakub, B. T. High-efficiency output pressure performance using capacitive micromachined ultrasonic transducers with substrate-embedded springs. *Sensors* **18**, 2520 (2018).
23. Dew, E. B., Kashani Ilkhechi, A., Maadi, M., Haven, N. J. M. & Zemp, R. J. Outperforming piezoelectric ultrasonics with high-reliability single-membrane CMUT array elements. *Microsyst. Nanoeng.* **8**, 59 (2022).
24. McEniery, C. M., Cockcroft, J. R., Roman, M. J., Franklin, S. S. & Wilkinson, I. B. Central blood pressure: current evidence and clinical importance. *Eur. Heart J.* **35**, 1719–1725 (2014).
25. HARRISON, E. G., ROTH, G. M. & HINES, E. A. Bilateral indirect and direct arterial pressures. *Circulation* **22**, 419–436 (1960).
26. Lee, B. C., Nikoozadeh, A., Park, K.-K. & Khuri-Yakub, B. T. Understanding CMUTs with substrate-embedded springs. in *2011 IEEE International Ultrasonics Symposium* 1008–1011 (IEEE, 2011).
27. Kim, H. Y. et al. Giant Pressure Output Efficiency of Capacitive Micromachined Ultrasonic Transducers Using Nano-Silicon-Springs. in *2022 IEEE International Ultrasonics Symposium (IUS)* vol. 2022-October 1–4 (IEEE, 2022).
28. Huang, Y. et al. Capacitive micromachined ultrasonic transducers with piston-shaped membranes: fabrication and experimental characterization. *IEEE Trans. Ultrason Ferroelectr. Freq. Control* **56**, 136–145 (2009).
29. Seok, C., Wu, X., Yamaner, F. Y. & Oralkan, O. A front-end integrated circuit for a 2D capacitive micromachined ultrasound transducer (CMUT) array as a noninvasive neural stimulator. in *2017 IEEE International Ultrasonics Symposium (IUS)* 1–4 (IEEE, 2017).
30. Bhuyan, A. et al. Integrated circuits for volumetric ultrasound imaging with 2-D CMUT Arrays. *IEEE Trans. Biomed. Circuits Syst.* **7**, 796–804 (2013).
31. Savoia, A. S. et al. A 3D packaging technology for acoustically optimized integration of 2D CMUT arrays and front end circuits. in *2017 IEEE International Ultrasonics Symposium (IUS)* 1–4 (IEEE, 2017).
32. Kil, H.-J. & Park, J.-W. Carotid artery monitoring patch using a supercapacitive pressure sensor with piezoelectricity. *Nano Energy* **114**, 108636 (2023).
33. Murray, C. S. G., Nahar, T., Kalashyan, H., Becher, H. & Nanda, N. C. Ultrasound assessment of carotid arteries: current concepts, methodologies, diagnostic criteria, and technological advancements. *Echocardiography* **35**, 2079–2091 (2018).
34. Kenny, J. -ÈS. et al. A novel, hands-free ultrasound patch for continuous monitoring of quantitative Doppler in the carotid artery. *Sci. Rep.* **11**, 7780 (2021).
35. Bhuyan, A. et al. Miniaturized, wearable, ultrasound probe for on-demand ultrasound screening. in *2011 IEEE International Ultrasonics Symposium* 1060–1063 (IEEE, 2011). <https://doi.org/10.1109/ULTSYM.2011.0260>.
36. Apte, N., Vaithilingam, S., Sarioglu, A. F., Kupnik, M. & Khuri-Yakub, B. T. Large area 1D CMUT phased arrays for multi-modality ultrasound imaging. in *2011 IEEE International Ultrasonics Symposium* 612–615 (IEEE, 2011). <https://doi.org/10.1109/ULTSYM.2011.0148>.
37. Park, K. K., Oralkan, O. & Khuri-Yakub, B. T. A comparison between conventional and collapse-mode capacitive micromachined ultrasonic transducers in 10-MHz 1-D arrays. *IEEE Trans. Ultrason Ferroelectr. Freq. Control* **60**, 1245–1255 (2013).
38. Wang, C. et al. Monitoring of the central blood pressure waveform via a conformal ultrasonic device. *Nat. Biomed. Eng.* **2**, 687–695 (2018).

Acknowledgements

This work was supported by the National Research Foundation of Korea (NRF) grant funded by the Korea government (MSIT) (RS-2024-00341714 to B.C.L.), the internal program of the Korea Institute of Science and Technology (2E33141 to H.K. and B.C.L., 2E3312H to B.C.L.), and the Korea Medical Device Development Fund grant funded by the Korea government (the Ministry of Science and ICT, the Ministry of Trade, Industry and Energy, the Ministry of Health & Welfare, the Ministry of Food and Drug Safety) (RS-2023-00254676 to W.L. and B.C.L.).

Author contributions

D.-H. Kang, S.C., BT K.-Y., and B.C.L. conceived and designed the research. H.Y.K. and B.C.L. performed the simulations. D.-H. Kang, S.C., H.Y.K., S.S., and B.C.L. designed and performed all the fabrication and device measurements. D.-H. Kang, S.C., D.H. Kim, B.J., Y.S.L., E.-A.P., W.L., and B.C.L. performed all the clinical studies. D.-H. Kang, S.C., E.-A.P., W.L., H.K., M.I., J.-W.J., and B.C.L. analysed the data. J.-W.J. and B.C.L. supervised the research and are project administrators. D.-H. Kang and S.C. initially wrote the paper. All authors provided active and valuable discussions and feedback on the manuscript.

Competing interests

The authors declare no competing interests.

Additional information

Supplementary information The online version contains supplementary material available at <https://doi.org/10.1038/s41467-025-61903-x>.

Correspondence and requests for materials should be addressed to Jae-Woong Jeong or Byung Chul Lee.

Peer review information *Nature Communications* thanks Monica La Mura, Zhuo Li, and the other anonymous reviewer(s) for their contribution to the peer review of this work. A peer review file is available.

Reprints and permissions information is available at <http://www.nature.com/reprints>

Publisher's note Springer Nature remains neutral with regard to jurisdictional claims in published maps and institutional affiliations.

Open Access This article is licensed under a Creative Commons Attribution-NonCommercial-NoDerivatives 4.0 International License, which permits any non-commercial use, sharing, distribution and reproduction in any medium or format, as long as you give appropriate credit to the original author(s) and the source, provide a link to the Creative Commons licence, and indicate if you modified the licensed material. You do not have permission under this licence to share adapted material derived from this article or parts of it. The images or other third party material in this article are included in the article's Creative Commons licence, unless indicated otherwise in a credit line to the material. If material is not included in the article's Creative Commons licence and your intended use is not permitted by statutory regulation or exceeds the permitted use, you will need to obtain permission directly from the copyright holder. To view a copy of this licence, visit <http://creativecommons.org/licenses/by-nc-nd/4.0/>.

© The Author(s) 2025